Towards Resilient Operation of Multi-Microgrids: An MISOCP-Based Frequency-Constrained Approach

Amin Gholami* and Xu Andy Sun†

H. Milton Stewart School of Industrial and Systems Engineering

Georgia Institute of Technology

Abstract

High penetration of distributed energy resources (DERs) is transforming the paradigm in power system operation. The ability to provide electricity to customers while the main grid is disrupted has introduced the concept of microgrids (μGs) with many challenges and opportunities. Emergency control of dangerous transients caused by the transition between the grid-connected and island modes in μGs is one of the main challenges in this context. To address this challenge, this paper proposes a comprehensive optimization and real-time control framework for maintaining frequency stability of multi-μG networks under an islanding event and for achieving optimal load shedding and network topology control with AC power flow constraints. The paper also develops a strong mixed-integer second-order cone programming (MISOCP)-based reformulation and a cutting plane algorithm for scalable computation. We believe this is the first time in the literature that such a framework for multi-μG network control is proposed, and its effectiveness is demonstrated with extensive numerical experiments.

Index terms— Islanding, microgrid, mixed-integer second order cone programming, resilience, under frequency load shedding.

1 Introduction

Microgrids (μGs), as building blocks of smart distribution grids, provide a unique infrastructure for integrating a wide range of distributed energy resources (DERs) with different static and dynamic characteristics. They are able to operate in island mode and energize a portion of the grid while the main grid is down. This islanding capability of μGs is highly beneficial for both customers and electric utilities, especially in areas with frequent electrical outages. Although dynamic islanding is one of the basic objectives of building a μG, IEEE Std. 929-2000 [1] and IEEE Std. 1547.7-2013 [2] mandate that DERs shall detect the unintentional island mode and cease to energize the grid within two seconds, mainly due to safety concerns as well as complying with conventional control/protection schemes. Operation of DERs during intentional islanding has also been under consideration for future revisions of IEEE Std. 1547. Based on the current practices and standards, blackouts in μGs seem inevitable in the event of islanding (especially an unscheduled islanding which may occur subsequent to detection of abnormal conditions at the interconnection(s)).

Intuitively, the disconnection of DERs is not an ideal solution, particularly in a restructured environment where electric utilities compete to provide a more reliable service to

*a.gholami@gatech.edu

†andy.sun@isye.gatech.edu

customers. In this context, a recent draft standard for interoperability of DERs in 2017 has provided some guidance on scheduled and unscheduled islanding processes [3]. This draft standard defines an intentional local island as any portion of the grid that is totally within the bounds of a local power grid (e.g., a μG), and further states that DERs may have to adjust several settings which shall be enabled only when the intentional island is isolated from the main grid. This standard calls for adaptive protection and control schemes to be used in such circumstances. Our paper is motivated by this need, and is aimed at providing a practical solution to the islanding process in modern distribution networks which are comprised of multiple μGs, referred to as multi-microgrid (multi-μG) networks.

In a similar vein, [4–6] acknowledge that the current practice of disconnecting DERs following a disturbance is no longer a reliable solution. Specifically, reference [4] proposes an under frequency load shedding (UFLS) scheme to be used subsequent to islanding in a distribution system. This scheme sheds an optimal number of loads based on a set of criteria including frequency, rate of change of frequency, customers' willingness to pay, and load histories. The authors in [5] investigate autonomous operation of a distribution system as an individual μG. The paper demonstrates the transient behavior of such a μG due to preplanned and unplanned islanding processes. The authors also emphasize that future studies should develop control strategies/algorithms for multiple electronically interfaced DERs to achieve optimum response in terms of stability. In [6], a controller for distributed generation (DG) inverters is designed for both grid-connected and intentional islanding modes. Moreover, an islanding-detection algorithm is developed in order to switch between the two modes.

On the other hand, the operation of multi-μGs has been studied in the literature from different perspectives, such as their on-line dynamic security assessment [7], interactive control for guaranteed small signal stability [8], transient stability assessment [9], electricity market operator design [10], hierarchical outage management [11], and self-healing [12] to name a few.

In this paper, we propose a novel framework for the resilient operation of multi-μG networks after a scheduled or unscheduled islanding in a distribution system. The framework is strategically designed in two parts. In the first part, we develop a near real-time decision support tool which is used to determine the optimal reconfiguration of the multi-μG network, cooperation between μGs (sharing their resources), new operating point of dispatchable DERs, and emergency load curtailments (if necessary). The second part of the framework pertains to the real-time monitoring and control of multi-μGs based on the outcomes of the decision support tool. The present paper is a significant extension to our recent work [13] on a single μG operation. Specifically, the main contributions of this paper are summarized below.

- We formulate the real-time resilient operation, including optimal power flow, optimal load shedding, and optimal topology reconfiguration, of a multi-μG network as a mixed-integer nonlinear programming (MINLP) problem. Then, we propose a mixed-integer second order cone programming (MISOCP) relaxation to this problem, which considerably improves the computational efficiency of our control framework and renders it scalable in practical systems.

- We derive necessary constraints for keeping the nadir and steady state frequency of the network within the permissible ranges, and introduce a new reformulation for frequency limitation constraints. This reformulation implicitly guarantees the frequency stability of the network after dangerous transients such as islanding.

- We develop a set of valid inequalities and a separation scheme for incorporating the frequency constraints in the operation of a multi-μG network, and based on that, we establish a cutting-plane approach to eliminate the frequency violations in a computationally effective way.

The rest of our paper is organized as follows. Section 2 introduces a resilient multi-μG network and gives an overview of the proposed scheme. The frequency response of multi-μGs to an islanding process is discussed in Section 3. In Section 4, a basic MINLP model for the real-time resilient operation of multi-μGs is presented. Section 5 is devoted to solution methodology, including the MISOCP relaxation and cutting plane algorithm. Section 6 exhibits the efficiency of the novel approach using an illustrative case study, and finally, the paper concludes with Section 7.

2 Resilient Operation of Multi-μGs

2.1 Structure of a Multi-μG Network

A distribution network may experience a scheduled islanding due to several reasons such as enhanced reliability, economic dispatch decisions for self-supply, pre-emptive action prior to inclement weather, etc. Moreover, unscheduled islanding happens subsequent to the detection of abnormal conditions at the interconnection(s) [3]. In either case, the distribution system can be further partitioned into multiple μGs, thereby improving the resilience of the system. Fig. 1 depicts a distribution network under such circumstances. As can be seen in this example, the distribution network is composed of four μGs, where each μG is connected to the rest of the system through the point of common coupling (PCC). Note that μGs in a multi-μG network are commonly integrated via voltage-source-converter-(VSC)-based interfaces at the PCC, and the behavior of each μG is characterized by the control scheme of its interface [14]. PCCs are commonly equipped with intelligent electronic devices (IEDs) with synchrophasor capability [7]. A communication network connects the IEDs to the distribution management system (DMS). Note that the resilience of this communication infrastructure (notably during an unscheduled outage) is of paramount importance to operators' situational awareness.

In Fig. 1(a), a set of buses (white fill in the figure), namely linking buses, are not categorized to any μG. Additionally, the lines (dashed/dotted in Fig. 1(a), or equivalently l_1 to l_5 in Fig. 1(b)) between such buses, namely linking lines, are equipped with switching relays, enabling various configurations for the multi-μG network. This portion of the distribution network that consists of the linking buses and linking lines is called the *linking grid*. Fig. 1(b) illustrates the linking grid associated with the multi-μG network of Fig. 1(a). Finally, the buses by which each μG is connected to the linking grid (gray fill in the figure) are called boundary buses.

2.2 Overview of the Proposed Resilient Operation Scheme

The general framework of the proposed resilience management scheme is illustrated in Fig. 2. This framework can be divided into two stages: i) near real-time decision support tool, and ii) real-time monitoring and control. In the first stage, the distribution system operator (DSO) leverages the state estimation (SE) module and obtains the input parameters of an optimization model. These data include the generation/consumption level of DERs/Loads,

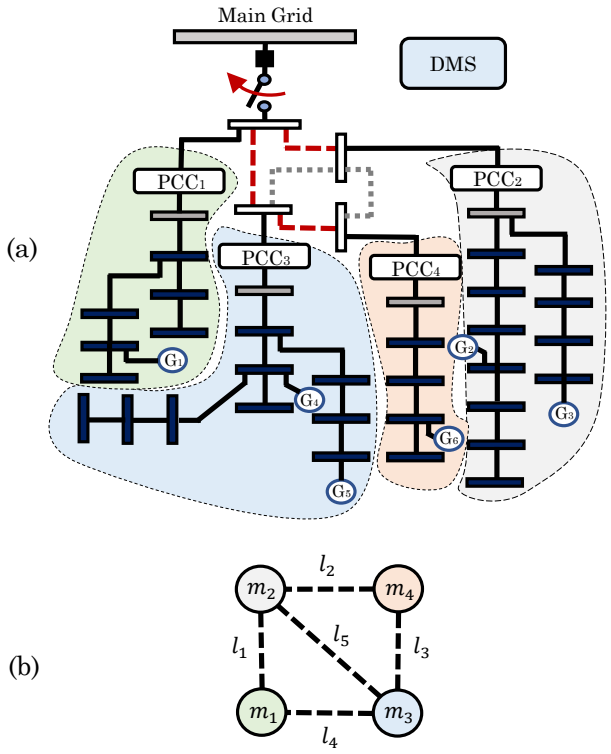

Figure 1: Schematic diagram of a distribution system under islanding. (a) Multi-μG network. (b) Linking grid.

real and reactive power exchange at PCCs, and the status of the circuit breakers (i.e., network topology). Subsequently, the optimization model is solved and the following resilient operation strategies are determined: optimal configuration of the linking network, cooperation between μGs (sharing their DERs), new operating point of dispatchable DERs, and emergency load curtailments (if necessary). Note that the frequency limitations of the system are embedded in the optimization model to ensure the frequency stability of multi-μGs following the islanding event. In the next step, a look-up table is generated based on the results of the optimization model. On the other side, in the second stage, the status of the main circuit breaker (i.e., the islanding status of the distribution network) is monitored using indication data. If an unscheduled/scheduled islanding happens, the pre-specified strategies will be implemented in the multi-μG network.

The principal focus of this paper is on the first stage (left-hand side of Fig. 2), i.e., developing a near real-time decision support tool that will be thoroughly discussed in the following sections. The second stage (right-hand side of Fig. 2) corresponds to the mechanisms for implementing such decisions. The details of these mechanisms, which are enabled by synchrophasor technology, go beyond the scope of this paper.

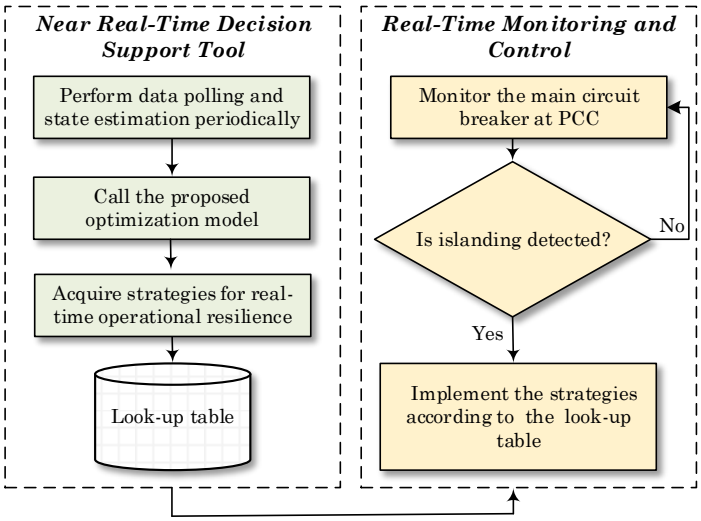

Figure 2: The general framework of the proposed resilient operation approach.

3 Frequency Response of Multi-μGs Subsequent to Islanding

In this section, we will derive the steady-state and nadir frequencies of a multi-μG network subsequent to an imbalance between real power generation and consumption. Later in Section 4.5, we will use these two metrics to construct our proposed frequency constraints, ensuring that they will remain in the permissible range during the transition between the grid-connected and island modes.

3.1 Inertial Response

As mentioned earlier, μGs in a multi-μG network are integrated via VSC-based interfaces at the PCC. Meanwhile, VSC-based interfaces are controlled in such a way that they emulate the behavior of conventional synchronous machines [9]. Inspired by this fact, let us first focus on inertial response of μGs. Suppose $\mathcal{M}$ is the set of all μGs in the multi-μG network. The artificial swing equation describes the inertial frequency dynamics of each $m \in \mathcal{M}$,

$$\frac{d\Delta\omega_m}{dt} = \frac{1}{2H_m}\left(\Delta P_m^M - \Delta P_m^E\right), \tag{1}$$

where $\Delta\omega_m$ is the frequency deviation in p.u.; H_m is the artificial inertia constant in seconds; ΔP_m^M and ΔP_m^E are the mechanical and electrical power deviations in p.u., respectively. Based on (1), modeling interconnected μGs can be realized by the so-called aggregation method [15]. Without loss of generality, we assume that for each $m \in \mathcal{M}$, equation (1) is per-unitized based on a common power, S_{Base}. We define the center of inertia (COI) frequency as

$$\omega_{COI} := \frac{\sum\limits_{m\in\mathcal{M}} H_m\omega_m}{\sum\limits_{m\in\mathcal{M}} H_m}. \tag{2}$$

Proposition 1. *The swing equation of a fictitious equivalent generator whose frequency is equal to ω_{COI} has the same form as*

$$\frac{d\Delta\omega_{COI}}{dt} = \frac{1}{2H_a}\left(\Delta P_a^M - \Delta P_a^E\right), \tag{3}$$

where H_a, ΔP_a^M, and ΔP_a^E are defined below

$$H_a := \sum_{m\in\mathcal{M}} H_m, \tag{4}$$

$$\Delta P_a^M := \sum_{m\in\mathcal{M}} \Delta P_m^M,\ \Delta P_a^E := \sum_{m\in\mathcal{M}} \Delta P_m^E. \tag{5}$$

Proof. A complete proof of this basic result cannot be easily located in the literature. Therefore, we provide one here. Consider a small deviation from the initial value in (2), i.e., $\Delta\omega_{COI} := \omega_{COI} - \omega_{COI}^0$ and $\Delta\omega_m := \omega_m - \omega_m^0$, and take derivative of its both sides with respect to t:

$$\frac{d\Delta\omega_{COI}}{dt} = \frac{\sum\limits_{m\in\mathcal{M}} H_m \frac{d\Delta\omega_m}{dt}}{\sum\limits_{m\in\mathcal{M}} H_m}. \tag{6}$$

Then, re-arrange (1) as

$$H_m\frac{d\Delta\omega_m}{dt} = \frac{1}{2}\left(\Delta P_m^M - \Delta P_m^E\right). \tag{7}$$

Now substitute (7) in (6), as

$$\frac{d\Delta\omega_{COI}}{dt} = \frac{\sum\limits_{m\in\mathcal{M}} \frac{1}{2}\left(\Delta P_m^M - \Delta P_m^E\right)}{\sum\limits_{m\in\mathcal{M}} H_m}. \tag{8}$$

With the definition of (4)-(5), we get (3). □

In the rest of the paper, the COI frequency is simply denoted by ω instead of ω_{COI}.

3.2 Droop Response

Now we construct the aggregated system frequency response (SFR) model of a multi-μG network as depicted in Fig. 3. In this model, the transfer function $\frac{1}{2H_a s+D}$ in the forward path represents the swing equation (3) as well as the frequency-dependent behavior of the loads which is lumped into a single damping constant D. In this paper, this damping constant D is assumed to remain unchanged while aggregating different μGs. Different feedback loops in Fig. 3 model the contribution of each μG to the droop control of the multi-μG network [15]. For each $m \in \mathcal{M}$, R_m is the droop constant of the VSC; T_m and T'_m are the corresponding time constants.

In general, the order of this SFR model is $|\mathcal{M}| + 1$. In particular, however, we are interested in the steady state and nadir outputs of the SFR model. It can be shown that the steady state output of this general-order model is not a function of the time constant T'_m. Moreover, the results of a sensitivity analysis on the parameters of a similar SFR model confirms that the nadir frequency is less sensitive to T'_m [16]. Accordingly, we assume

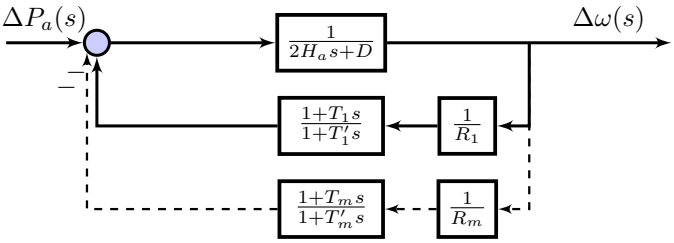

Figure 3: Block diagram of the aggregated SFR model.

identical values of T_m' for all μGs in the multi-μG network, i.e., $T' := T_m', \forall m \in \mathcal{M}$. Consequently, the transfer function of the aggregated SFR model can be written as (9), with the additional parameters defined in (10):

$$\mathcal{H}(s) = \frac{1 + T's}{2H_a T' \left(s^2 + 2\xi\omega_n s + \omega_n^2\right)}, \tag{9}$$

$$\omega_n := \sqrt{\frac{D + 1/R_a}{2H_a T'}},\ \xi := \frac{2H_a + T'D + K_a}{2\sqrt{2H_a T' \left(D + 1/R_a\right)}}, \tag{10a}$$

$$\frac{1}{R_a} := \sum_{m \in \mathcal{M}} \frac{1}{R_m}, K_a := \sum_{m \in \mathcal{M}} \frac{T_m}{R_m}, \tag{10b}$$

where $\Delta P_a(s)$ is the disturbance power in the multi-μG.

3.3 Steady State and Nadir Frequencies at COI

In general, the dynamic behavior of the aggregated SFR model can be described by two parameters ξ and ω_n. If $\xi = 0$, we will have an oscillatory system where the transient response will not die out. If $\xi \in (0, 1)$, the transient frequency response is oscillatory (under-damped). When $\xi = 1$, we are in the critically-damped condition, and finally, if $\xi \in (1, +\infty)$, the frequency response will be over-damped. We shall now analyze the frequency response of the system to the unit-step input, i.e., $\Delta P_a(s) = 1/s$ for three cases: the under-damped, critically-damped, and over-damped cases.

Proposition 2. *In the under-damped case, the steady state and nadir COI frequencies of a multi-μG network after a unit-step disturbance can be obtained by (11) and (12), respectively, i.e.,*

$$\Delta\omega(t^{ss}) = \frac{1}{D + 1/R_a}, \tag{11}$$

$$\Delta\omega\left(t^N\right) = \frac{1}{D + 1/R_a}\left(1 + \sqrt{\frac{T' - R_a K_a}{2H_a R_a}} e^{-\xi\omega_n t^N}\right), \tag{12}$$

where t^N in (12) can be calculated as follows:

$$t^N = \begin{cases} \frac{1}{\omega_r}\left(\pi - \tan^{-1}\left(\frac{\omega_r T'}{1 - \xi\omega_n T'}\right)\right), & \text{if } \xi\omega_n T' < 1, \\ \frac{\pi}{2\omega_r}, & \text{if } \xi\omega_n T' = 1, \\ \frac{1}{\omega_r}\left(\tan^{-1}\left(\frac{\omega_r T'}{\xi\omega_n T' - 1}\right)\right), & \text{if } \xi\omega_n T' > 1. \end{cases} \tag{13}$$

Additionally, in the critically-damped and over-damped cases, the nadir COI frequency is equal to the steady state COI frequency, and both can be calculated according to (11).

Proof. In the under-damped case, the poles of the system are $s_{1,2} = -\xi\omega_n \pm j\omega_r$, where $\omega_r = \omega_n\sqrt{1-\xi^2}$ is the damped natural frequency and $j = \sqrt{-1}$ is the imaginary unit. In this case, the unit-step response is

$$\Delta\omega(t) = \frac{1}{2H_a T'}\Big(\frac{1}{\omega_n^2} + \frac{e^{-\xi\omega_n t}}{\omega_r}\Big(T'\sin(\omega_r t) - \frac{1}{\omega_n}\sin(\omega_r t + \phi)\Big)\Big), \tag{14}$$

where $\phi := \tan^{-1}(\frac{\sqrt{1-\xi^2}}{\xi})$. By definition, the steady state frequency is equal to $\Delta\omega(t^{ss}) := \lim_{t\to+\infty}\Delta\omega\,(t)$, which leads to (11). The time when the frequency nadir happens (when the lowest frequency is reached before the frequency starts to recover) can be calculated by solving the optimization problem $t^N := \min\{t : \frac{d\Delta\omega(t)}{dt} = 0, t \in \mathbb{R}_{++}\}$. The closed-form solution to this problem is equal to (13). Additionally. substitution of t^N in (14) yields (12). Observe that when the two poles of the transfer function (9) are nearly equal, i.e., $s_{1,2} = -\omega_n$, the system is approximated by a critically-damped one. Moreover, in the over-damped case, the two poles of the transfer function are negative real and unequal, i.e., $s_{1,2} = -\xi\omega_n \pm \omega_n\sqrt{\xi^2-1}$. In the last two cases, no overshoot or undershoot is observed in the transient response of the system, and consequently, the nadir frequency is equal to the steady state frequency which is identical to (11). □

The interested reader is referred to Proposition 3 in [17] for similar results under different settings. Now we are ready to adopt the steady-state and nadir frequencies at COI in order to build our optimization model for the resilient operation of a multi-μG network.

4 Resilient Operation Problem Formulation

Consider a linking grid $\tilde{\mathcal{N}} = (\tilde{\mathcal{B}}, \tilde{\mathcal{L}})$, where $\tilde{\mathcal{B}}$ and $\tilde{\mathcal{L}}$ denote the set of linking buses and linking lines, respectively. We assume that the distribution network under study is comprised of a set of μGs, i.e., $m \in \mathcal{M}$, where each μG is modeled as a disjoint network $\mathcal{N}_m = (\mathcal{B}_m, \mathcal{L}_m)$. Without loss of generality, we assume only one PCC for each μG, and the corresponding boundary bus is denoted by $\hat{\mathcal{B}}$. In this section, we aim to introduce an optimization model which is able to determine the optimal resilience improvement strategy, including optimal load shedding and network topology control with AC power flow, in the wake of a scheduled/unscheduled islanding in a multi-μG network. Our model is formulated as follows.

4.1 Objective Function

The objective function (15) is to minimize the total load shedding cost in all μGs:

$$\min \sum_{m\in\mathcal{M}}\sum_{i\in\mathcal{B}_m} \lambda_{mi}^{VOLL}\,(1 - x_{mi})\,\bar{p}_{mi}^{D}, \tag{15}$$

where λ_{mi}^{VOLL} is the value of lost load (VOLL) in μG m and bus i; $\bar{p}_{mi}^{D}$ is the pre-islanding active power consumption obtained from state estimation (SE); and x_{mi} is a binary variable indicating the status of such a load after islanding happens.

4.2 Real-Time AC Power Flow Limitations in μGs

The set of constraints (16)-(25) which are defined for each $m \in \mathcal{M}$ guarantee the AC power flow security of each μG after the islanding event. Let G_{mij} and B_{mij} be the conductance and susceptance of line (i,j) in μG m; and f^P_{mij} and f^Q_{mij} be the active and reactive flow of that line. Additionally, let p^G_{mg} and q^G_{mg} be the active and reactive power output of DER g in μG m; and similarly, p^D_{mi} and q^D_{mi} be the active and reactive power consumption of the load at bus i in μG m. We define V_{mi} and θ_{mi} as the voltage magnitude and angle of bus i in μG m. Finally, ΔP_m and ΔQ_m denote the active and reactive power exchange between the μG m and the linking grid (through the VSC). Based on this notation, constraints (16) and (17) model the active and reactive power balance within each μG. Similarly, constraints (18) and (19) are related to the active and reactive power balance at the boundary buses. Note that $\mathcal{O}$ in these equations is the mapping of the set of DERs into the set of buses. The set of equations (20)-(23) constitute the AC power flow equations, line flow limits, and voltage bounds in each μG. Finally, active and reactive power demands at different buses are modeled by the voltage-dependent ZIP model (24) and (25), where κ^{PI}, κ^{PC}, and κ^{PP} denote the coefficients of constant impedance, constant current, and constant power terms in active power loads, respectively. These coefficients are defined in the same way for reactive power loads.

$$\sum_{g:(g,i)\in\mathcal{O}_m} p^G_{mg} - x_{mi}p^D_{mi} = \sum_{(i,j)\in\mathcal{L}_m} f^P_{mij}, \forall i \in \mathcal{B}_m \tag{16}$$

$$\sum_{g:(g,i)\in\mathcal{O}_m} q^G_{mg} - x_{mi}q^D_{mi} = \sum_{(i,j)\in\mathcal{L}_m} f^Q_{mij}, \forall i \in \mathcal{B}_m \tag{17}$$

$$\sum_{g:(g,i)\in\mathcal{O}_m} p^G_{mg} - x_{mi}p^D_{mi} + \Delta P_m = \sum_{(i,j)\in\mathcal{L}_m} f^P_{mij}, \forall i \in \hat{\mathcal{B}}_m \tag{18}$$

$$\sum_{g:(g,i)\in\mathcal{O}_m} q^G_{mg} - x_{mi}q^D_{mi} + \Delta Q_m = \sum_{(i,j)\in\mathcal{L}_m} f^Q_{mij}, \forall i \in \hat{\mathcal{B}}_m \tag{19}$$

$$\begin{aligned} f^P_{mij} = {} & G_{mij}\Big(V^2_{mi} - V_{mi}V_{mj}\cos\left(\theta_{mi}-\theta_{mj}\right)\Big) \\ & - B_{mij}V_{mi}V_{mj}\sin\left(\theta_{mi}-\theta_{mj}\right), \forall (i,j) \in \mathcal{L}_m \end{aligned} \tag{20}$$

$$\begin{aligned} f^Q_{mij} = {} & -B_{mij}\Big(V^2_{mi} - V_{mi}V_{mj}\cos\left(\theta_{mi}-\theta_{mj}\right)\Big) \\ & - G_{mij}V_{mi}V_{mj}\sin\left(\theta_{mi}-\theta_{mj}\right), \forall (i,j) \in \mathcal{L}_m \end{aligned} \tag{21}$$

$$f^P_{mij} + f^P_{mji} \leq f^{\max}_{mij}, \ \forall (i,j) \in \mathcal{L}_m \tag{22}$$

$$V^{\min}_{mi} \leq V_{mi} \leq V^{\max}_{mi}, \ \forall i \in (\mathcal{B}_m \cup \hat{\mathcal{B}}_m) \tag{23}$$

$$p^D_{mi} = \overline{p}^D_{mi}\Big(\kappa^{PI}_{mi}V^2_{mi} + \kappa^{PC}_{mi}V_{mi} + \kappa^{PP}_{mi}\Big), \forall i \in (\mathcal{B}_m \cup \hat{\mathcal{B}}_m) \tag{24}$$

$$q^D_{mi} = \overline{q}^D_{mi}\Big(\kappa^{QI}_{mi}V^2_{mi} + \kappa^{QC}_{mi}V_{mi} + \kappa^{QP}_{mi}\Big), \forall i \in (\mathcal{B}_m \cup \hat{\mathcal{B}}_m). \tag{25}$$

4.3 Real-Time AC Power Flow Limitations in the Linking Grid

Similarly, this group of constraints are associated with the AC power flow limitations of the linking grid. Here, line switching is available, therefore, Z_{mk} is a binary variable indicating the status of the linking line (m,k). It is worth mentioning that connection/disconnection of μGs to the linking grid is performed through the switchgear located at PCCs and line switching in the linking grid is commonly available through the distribution automation switches and isolators [7]. Let M_{mk} be a sufficiently large positive number. In these constraints, in terms of notation, we use tilde over the variables and parameters to make the difference between the linking grid and the rest of the distribution grid. In particular, equations (26) and (27) model the active and reactive power balance at external buses. The group of constraints (28)-(35) are associated with the AC power flow equations (where the lines are allowed to be switched on and off), line flow limits, and voltage bounds in the linking grid.

$$-\Delta P_m = \sum_{(m,k)\in\tilde{\mathcal{L}}} \tilde{f}^P_{mk},\ \forall m \in \mathcal{M} \tag{26}$$

$$-\Delta Q_m = \sum_{(m,k)\in\tilde{\mathcal{L}}} \tilde{f}^Q_{mk},\ \forall m \in \mathcal{M} \tag{27}$$

$$\begin{aligned}-\tilde{f}^P_{mk} + \tilde{G}_{mk}\Big(\tilde{V}_m^2 - \tilde{V}_m\tilde{V}_k\cos(\theta_m-\theta_k)\Big) - \tilde{B}_{mk}\tilde{V}_m\tilde{V}_k\sin(\theta_m-\theta_k)\\ + (1-Z_{mk})\,M_{mk} \geq 0,\ \forall (m,k)\in\tilde{\mathcal{L}}\end{aligned} \tag{28}$$

$$\begin{aligned}-\tilde{f}^P_{mk} + \tilde{G}_{mk}\Big(\tilde{V}_m^2 - \tilde{V}_m\tilde{V}_k\cos(\theta_m-\theta_k)\Big) - \tilde{B}_{mk}\tilde{V}_m\tilde{V}_k\sin(\theta_m-\theta_k)\\ - (1-Z_{mk})\,M_{mk} \leq 0,\ \forall (m,k)\in\tilde{\mathcal{L}}\end{aligned} \tag{29}$$

$$\begin{aligned}-\tilde{f}^Q_{mk} - \tilde{B}_{mk}\Big(V_m^2 - \tilde{V}_m\tilde{V}_k\cos(\theta_m-\theta_k)\Big) - \tilde{G}_{mk}\tilde{V}_m\tilde{V}_k\sin(\theta_m-\theta_k)\\ + (1-Z_{mk})\,M'_{mk} \geq 0,\ \forall (m,k)\in\tilde{\mathcal{L}}\end{aligned} \tag{30}$$

$$\begin{aligned}-\tilde{f}^Q_{mk} - \tilde{B}_{mk}\Big(V_m^2 - \tilde{V}_m\tilde{V}_k\cos(\theta_m-\theta_k)\Big) - \tilde{G}_{mk}\tilde{V}_m\tilde{V}_k\sin(\theta_m-\theta_k)\\ - (1-Z_{mk})\,M'_{mk} \leq 0,\ \forall (m,k)\in\tilde{\mathcal{L}}\end{aligned} \tag{31}$$

$$-\tilde{f}^{P,\max}_{mk} Z_{mk} \leq \tilde{f}^P_{mk} \leq \tilde{f}^{P,\max}_{mk} Z_{mk},\ \forall (m,k)\in\tilde{\mathcal{L}} \tag{32}$$

$$-\tilde{f}^{Q,\max}_{mk} Z_{mk} \leq \tilde{f}^Q_{mk} \leq \tilde{f}^{Q,\max}_{mk} Z_{mk},\ \forall (m,k)\in\tilde{\mathcal{L}} \tag{33}$$

$$\tilde{f}^P_{mk} + \tilde{f}^P_{km} \leq \tilde{f}^{P,Loss,\max}_{mk},\ \forall (m,k)\in\tilde{\mathcal{L}} \tag{34}$$

$$\tilde{V}^{\min}_m \leq \tilde{V}_m \leq \tilde{V}^{\max}_m,\ \forall i\in\tilde{\mathcal{B}},\ m\in\mathcal{M}. \tag{35}$$

4.4 DER Output Limitations and Binary Variable Declaration

Finally, (36)-(39) pertain to the limitations on the output of the generators and the declaration of binary variables. In these constraints, R^D, R^U, and $p^{G,0}$ are the ramp-down, ramp-up, and pre-islanding active power generation of DERs, respectively.

$$-R^D_{mg} \leq p^G_{mg} - p^{G,0}_{mg} \leq R^U_{mg},\ \forall g \in \mathcal{G}_m, m \in \mathcal{M} \tag{36}$$

$$p^{G,\min}_{mg} \leq p^G_{mg} \leq p^{G,\max}_{mg},\ \forall g \in \mathcal{G}_m, m \in \mathcal{M} \tag{37}$$

$$q^{G,\min}_{mg} \leq q^G_{mg} \leq q^{G,\max}_{mg},\ \forall g \in \mathcal{G}_m, m \in \mathcal{M} \tag{38}$$

$$x \in \{0,1\}^{|\mathcal{M}|\times|\mathcal{B}\cup\hat{\mathcal{B}}|},\ Z \in \{0,1\}^{|\tilde{\mathcal{L}}|}. \tag{39}$$

4.5 Frequency Constraints and Reformulation

In Section 3, we developed the steady-state and nadir frequencies of a multi-μG network subsequent to an imbalance between real power generation and consumption. Indeed, these are two important metrics which are employed to ensure the frequency security of the network. Therefore, we aim to keep these two metrics within the permissible range while the multi-μG network moves from the grid-connected mode to the island mode. Note that subsequent to the islanding process, the distribution network might be partitioned into different components (each component might include one or more μGs), and the frequency security limitations must be met for each component separately. We propose the following constraints for ensuring the frequency security of the multi-μG network for each $\mathcal{S} \subseteq \tilde{\mathcal{N}}, \mathcal{S} \neq \emptyset$:

$$\begin{aligned}\Delta\omega^{\min}_N \leq\ & \alpha_{\mathcal{S}} \sum_{m\in\tilde{\mathcal{B}}_{\mathcal{S}}} \left(-\Delta P^0_m + \sum_{i\in\mathcal{B}_m} (1-x_{mi})\, p^D_{mi}\right) \\ & + \mathcal{I}_M\left(\mathcal{S} \text{ is connected}\right) + \mathcal{I}_M\left(\mathcal{S} \text{ is isolated}\right),\end{aligned} \tag{40a}$$

$$\begin{aligned}\Delta\omega^{\max}_N \geq\ & \alpha_{\mathcal{S}} \sum_{m\in\tilde{\mathcal{B}}_{\mathcal{S}}} \left(-\Delta P^0_m + \sum_{i\in\mathcal{B}_m} (1-x_{mi})\, p^D_{mi}\right) \\ & - \mathcal{I}_M\left(\mathcal{S} \text{ is connected}\right) - \mathcal{I}_M\left(\mathcal{S} \text{ is isolated}\right),\end{aligned} \tag{40b}$$

$$\begin{aligned}\Delta\omega^{\min}_{ss} \leq\ & \beta_{\mathcal{S}} \sum_{m\in\tilde{\mathcal{B}}_{\mathcal{S}}} \left(-\Delta P^0_m + \sum_{i\in\mathcal{B}_m} (1-x_{mi})\, p^D_{mi}\right) \\ & + \mathcal{I}_M\left(\mathcal{S} \text{ is connected}\right) + \mathcal{I}_M\left(\mathcal{S} \text{ is isolated}\right),\end{aligned} \tag{40c}$$

$$\begin{aligned}\Delta\omega^{\max}_{ss} \geq\ & \beta_{\mathcal{S}} \sum_{m\in\tilde{\mathcal{B}}_{\mathcal{S}}} \left(-\Delta P^0_m + \sum_{i\in\mathcal{B}_m} (1-x_{mi})\, p^D_{mi}\right) \\ & - \mathcal{I}_M\left(\mathcal{S} \text{ is connected}\right) - \mathcal{I}_M\left(\mathcal{S} \text{ is isolated}\right),\end{aligned} \tag{40d}$$

where $\mathcal{I}_M$ is the indicator function whose value is equal to 0 if the condition is satisfied, and equal to a sufficiently large number, otherwise. Moreover, $\alpha_{\mathcal{S}}$ and $\beta_{\mathcal{S}}$ are the nadir and steady state values of the unit-step frequency response, which are calculated in (12) and (11), respectively. The use of subscript $\mathcal{S}$ in these two parameters emphasizes that they

should be calculated for each $\mathcal{S} \subseteq \tilde{\mathcal{N}}$, that is, the associated parameters H_a, R_a, and K_a are obtained by (4) and (10b), where $m \in \mathcal{M}$ is replaced by $m \in \tilde{\mathcal{B}}_{\mathcal{S}}$. Note that $\Delta\omega_N^{\min}/\Delta\omega_N^{\max}$ and $\Delta\omega_{ss}^{\min}/\Delta\omega_{ss}^{\max}$ denote the lower/upper bound on the nadir and steady state frequencies, respectively. Moreover, ΔP_m^0 denotes the pre-islanding power exchange between μG m and the linking grid. In (40), the first term on the right-hand side of the inequities is indeed the multiplication of the unit-step response by the post-islanding net power mismatch (i.e., pre-islanding power exchange minus the amount of post-islanding load shedding). Let us further investigate these frequency security constraints by defining

$$\tilde{\mathcal{L}}(\mathcal{S}) := \{(m,k) \in \tilde{\mathcal{L}} :\ m,k \in \tilde{\mathcal{B}}_{\mathcal{S}},\ m > k\}, \tag{41a}$$

$$\delta(\mathcal{S}) := \{(m,k) \in \tilde{\mathcal{L}} :\ m \in \tilde{\mathcal{B}}_{\mathcal{S}},\ k \notin \tilde{\mathcal{B}}_{\mathcal{S}},\ m > k\}. \tag{41b}$$

Given a subgraph $\mathcal{S}$ of $\tilde{\mathcal{N}}$, $\tilde{\mathcal{L}}(\mathcal{S})$ in (41a) denotes the set of edges in the subgraph $\mathcal{S}$, i.e., the set of edges in $\tilde{\mathcal{L}}$ whose both ends are in $\tilde{\mathcal{B}}_{\mathcal{S}}$. Additionally, (41b) describes the cutset $\delta(\mathcal{S})$, i.e., the set of edges that have exactly one end in $\tilde{\mathcal{B}}_{\mathcal{S}}$. Now, we will provide an equivalent reformulation for (40) using a spanning tree characterization. This reformulation will help us verify the frequency constraints in each connected component of the grid. It also provides new insights into the way we interpret the frequency constraints. We will focus on the inequality (40a); (40b)-(40d) can be similarly analyzed.

Proposition 3. *Inequality (40a) is equivalent to (42a), that is,*

$$\begin{aligned}\Delta\omega_N^{\min} \le \alpha_{\mathcal{S}} \sum_{m\in\tilde{\mathcal{B}}_{\mathcal{S}}} \Big(-\Delta P_m^0 + \sum_{i\in\mathcal{B}_m} (1-x_{mi})\, p_{mi}^D\Big) \\ + \min\{0 : (43a) - (43d)\} + \sum_{(m,k)\in\delta(\mathcal{S})} (Z_{mk}) M_N, \\ \forall \mathcal{S} \subseteq \tilde{\mathcal{N}}, \mathcal{S} \neq \emptyset\end{aligned} \tag{42a}$$

where

$$u_{mk} \le Z_{mk},\ \forall (m,k) \in \tilde{\mathcal{L}}(\mathcal{S}), \tag{43a}$$

$$\sum_{(m,k)\in\tilde{\mathcal{L}}(\mathcal{S})} u_{mk} = |\tilde{\mathcal{B}}_{\mathcal{S}}| - 1, \tag{43b}$$

$$\sum_{(m,k)\in\delta(\mathcal{S})} u_{mk} \ge 1,\ \forall \mathcal{S} \subseteq \tilde{\mathcal{N}}, \mathcal{S} \neq \emptyset, \tilde{\mathcal{N}}, \tag{43c}$$

$$u_{mk} \in \{0,1\},\ \forall (m,k) \in \tilde{\mathcal{L}}(\mathcal{S}). \tag{43d}$$

Proof. The minimization problem embedded in (42a) has an optimal value equal to 0 if there exists an spanning tree in $\mathcal{S}$. Otherwise, the problem is infeasible and the objective value will be equal to $+\infty$, making (42a) redundant. Here, we use the definition of a tree as a connected graph containing $n-1$ edges (n is the number of nodes in the graph). Accordingly, (43a) ensures that the spanning tree is a subgraph of $\mathcal{S}$. Additionally, (43b) and (43c) guarantee that the spanning tree has $|\tilde{\mathcal{B}}_{\mathcal{S}}| - 1$ edges and satisfies the connectivity requirement, respectively. Finally, the last term in (42a) ensures that $\mathcal{S}$ is a component. □

Note that both (40) and their reformulation in the form of (42a) have an exponential number of constraints. We will propose a cutting-plane approach to deal with this issue in Section 5.

4.6 Overall MINLP Formulation

Before passing to solution methodology of the problem, let us review the overall MINLP formulation of the multi-μG resilient operation problem. The decision variables of this formulation are: i) the status of loads (x_{mi}); ii) the status of linking lines (Z_{mk}); iii) active and reactive flow of lines (f^P_{mij}, f^Q_{mij}, $\tilde{f}^P_{mk}$, $\tilde{f}^Q_{mk}$); iv) active and reactive power of DERs and loads (p^G_{mg}, q^G_{mg}, p^D_{mi}, q^D_{mi}); v) voltage magnitudes and angles (V_{mi}, θ_{mi}); vi) active and reactive power exchange between the μGs and the linking grid (ΔP_m, ΔQ_m); and vii) spanning tree variable (u_{mk}). For the sake of brevity, let $\mathcal{X}$ be the set of constraints (16)-(39) and let $\mathcal{F}$ represent the set of constraints in (40). Now, we introduce $\mathcal{MINLP}(\mathcal{X},\mathcal{F})$ as follows:

$$\vartheta = \min \sum_{m\in\mathcal{M}} \sum_{i\in\mathcal{B}_m} \lambda^{VOLL}_{mi} \left(1 - x_{mi}\right) \bar{p}^D_{mi}$$
$$\text{s.t.} \quad (16)\text{-}(40).$$

5 Solution Methodology

The formulation $\mathcal{MINLP}(\mathcal{X},\mathcal{F})$ is a nonconvex nonlinear optimization problem. Moreover, the developed frequency limitations in (40) as well as their equivalent reformulations in (42a) induce exponentially many constraints. In this section, we will address these challenges.

5.1 MISOCP Reformulation and Convexification

Observe that all the nonlinearity and nonconvexity of $\mathcal{MINLP}(\mathcal{X},\mathcal{F})$ stem from three sources: i) the nonlinear terms V^2_{mi}, $V_{mi}V_{mj}\cos\left(\theta_{mi}-\theta_{mj}\right)$, and $V_{mi}V_{mj}\sin\left(\theta_{mi}-\theta_{mj}\right)$ in constraints (20)-(21) and also the similar terms in (28)-(31), ii) the quadratic term V^2_{mi} in constraints (24)-(25), iii) the bilinear terms $x_{mi}p^D_{mi}$ and $x_{mi}q^D_{mi}$ in constraints (16)-(19) and (40). In this section, we will convexify/linearize the aforementioned terms, leading to an MISOCP relaxation of the multi-μG resilient operation problem.

5.1.1 MISOCP Relaxation of AC Power Flow Equations

Based on the recent development in SOCP relaxation of standard AC-OPF [18], we define the following auxiliary variables for each $(i,j)\in\mathcal{L}_m$ and $m\in\mathcal{M}$:

$$C_{mij} := V_{mi}V_{mj}\cos\left(\theta_{mi}-\theta_{mj}\right), \tag{44a}$$
$$S_{mij} := V_{mi}V_{mj}\sin\left(\theta_{mi}-\theta_{mj}\right). \tag{44b}$$

Observe that (44) implies (45), that is

$$C^2_{mij} + S^2_{mij} = C_{mii}C_{mjj}, \tag{45a}$$
$$S_{mij} = -S_{mji},\ C_{mij} = C_{mji}. \tag{45b}$$

Similarly, we define $\tilde{C}_{mk} := \tilde{V}_m\tilde{V}_k\cos(\theta_m-\theta_k)$ and $\tilde{S}_{mk} = \tilde{V}_m\tilde{V}_k\sin(\theta_m-\theta_k)$ for each $(m,k)\in\tilde{\mathcal{L}}$, and the following constraints will be inferred:

$$\tilde{C}^2_{mk} + \tilde{S}^2_{mk} = \tilde{C}_{mm}\tilde{C}_{kk}, \tag{46a}$$
$$\tilde{S}_{mk} = -\tilde{S}_{km},\ \tilde{C}_{mk} = \tilde{C}_{km}. \tag{46b}$$

Note that the convex relaxation of (45a) and (46a) are:

$$C_{mij}^2 + S_{mij}^2 \leq C_{mii} C_{mjj}, \tag{47a}$$

$$\tilde{C}_{mk}^2 + \tilde{S}_{mk}^2 \leq \tilde{C}_{mm} \tilde{C}_{kk}. \tag{47b}$$

With a change of variables for each $m \in \mathcal{M}$ and $(i,j) \in \mathcal{L}_m$, constraints (20) and (21) can be written as

$$f_{mij}^P = G_{mij}\Big(C_{mii} - C_{mij}\Big) - B_{mij} S_{mij}, \tag{48a}$$

$$f_{mij}^Q = -B_{mij}\Big(C_{mii} - C_{mij}\Big) - G_{mij} S_{mij}, \tag{48b}$$

and the voltage bound (23) for each $m \in \mathcal{M}$ and $i \in (\mathcal{B}_m \cup \hat{\mathcal{B}}_m)$ is transformed into

$$(V_{mi}^{\min})^2 \leq C_{mii} \leq (V_{mi}^{\max})^2. \tag{49}$$

Likewise, a change of variables for each $(m,k) \in \tilde{\mathcal{L}}$ leads to the constraints (50) as the counterparts of (28)-(31):

$$-\tilde{f}_{mk}^P + \tilde{G}_{mk}\Big(\tilde{C}_{mm} - \tilde{C}_{mk}\Big) - \tilde{B}_{mk}\tilde{S}_{mk} + (1 - Z_{mk})\, M_{mk} \geq 0, \tag{50a}$$

$$-\tilde{f}_{mk}^P + \tilde{G}_{mk}\Big(\tilde{C}_{mm} - \tilde{C}_{mk}\Big) - \tilde{B}_{mk}\tilde{S}_{mk} - (1 - Z_{mk})\, M_{mk} \leq 0, \tag{50b}$$

$$-\tilde{f}_{mk}^Q - \tilde{B}_{mk}\Big(\tilde{C}_{mm} - \tilde{C}_{mk}\Big) - \tilde{G}_{mk}\tilde{S}_{mk} + (1 - Z_{mk})\, M'_{mk} \geq 0, \tag{50c}$$

$$-\tilde{f}_{mk}^Q - \tilde{B}_{mk}\Big(\tilde{C}_{mm} - \tilde{C}_{mk}\Big) - \tilde{G}_{mk}\tilde{S}_{mk} - (1 - Z_{m,k})\, M'_{mk} \leq 0, \tag{50d}$$

and similarly the voltage bound (35) for each $m \in \mathcal{M}$ and $i \in \tilde{\mathcal{B}}$ can be written as:

$$(\tilde{V}_m^{\min})^2 \leq \tilde{C}_{mm} \leq (\tilde{V}_m^{\max})^2. \tag{51}$$

5.1.2 MISOCP Relaxation of ZIP Load Models

Using the SOCP auxiliary variables defined in Section 5.1.1, the ZIP load models (24) and (25) can be written as (52) for each $m \in \mathcal{M}$ and $i \in (\mathcal{B}_m \cup \hat{\mathcal{B}}_m)$, that is

$$p_{mi}^D = \overline{p}_{mi}^D\Big(\kappa_{mi}^{PI} C_{mii} + \kappa_{mi}^{PC}\sqrt{C_{mii}} + \kappa_{mi}^{PP}\Big), \tag{52a}$$

$$q_{mi}^D = \overline{q}_{mi}^D\Big(\kappa_{mi}^{QI} C_{mii} + \kappa_{mi}^{QC}\sqrt{C_{mii}} + \kappa_{mi}^{QP}\Big). \tag{52b}$$

The convex relaxation of these two constraints can be written as

$$\overline{p}_{mi}^D\Big(\kappa_{mi}^{PI} C_{mii} + \kappa_{mi}^{PC}\sqrt{C_{mii}} + \kappa_{mi}^{PP}\Big) - p_{mi}^D \geq 0, \tag{53a}$$

$$\overline{q}_{mi}^D\Big(\kappa_{mi}^{QI} C_{mii} + \kappa_{mi}^{QC}\sqrt{C_{mii}} + \kappa_{mi}^{QP}\Big) - q_{mi}^D \geq 0. \tag{53b}$$

Since the variable C_{mii} is bounded by the closed interval $[C_{mii}^{\min}, C_{mii}^{\max}]$, the convex relaxation (53) can be tighten by introducing the following two hyperplanes which pass through the end points for each $i \in (\mathcal{B}_m \cup \hat{\mathcal{B}}_m)$ and $m \in \mathcal{M}$:

$$p_{mi}^D - p_{mi}^{D,\min} \geq \frac{p_{mi}^{D,\max} - p_{mi}^{D,\min}}{C_{mii}^{\max} - C_{mii}^{\min}}\left(C_{mii} - C_{mii}^{\min}\right), \tag{54a}$$

$$q_{mi}^D - q_{mi}^{D,\min} \geq \frac{q_{mi}^{D,\max} - q_{mi}^{D,\min}}{C_{mii}^{\max} - C_{mii}^{\min}}\left(C_{mii} - C_{mii}^{\min}\right). \tag{54b}$$

Proposition 4. *Constraints (53a) and (53b) are SOCP representable in terms of C^2_{mii}.*

Proof. We focus on constraint (53a); constraint (53b) is similarly analyzed. First, we rearrange and square both sides of the constraint for each $i \in (\mathcal{B}_m \cup \hat{\mathcal{B}}_m)$ and $m \in \mathcal{M}$ such that

$$\kappa^{PC}_{mi} \sqrt{C_{mii}} \geq \frac{p^D_{mi}}{\overline{p}^D_{mi}} - \kappa^{PI}_{mi} C_{mii} - \kappa^{PP}_{mi} \tag{55}$$

$$\left(\kappa^{PC}_{mi}\right)^2 C_{mii} \geq \left(\frac{p^D_{mi}}{\overline{p}^D_{mi}} - \kappa^{PI}_{mi} C_{mii} - \kappa^{PP}_{mi}\right)^2. \tag{56}$$

Note that $C_{mii} = (\frac{C_{mii}+1}{2})^2 - (\frac{C_{mii}-1}{2})^2$, therefore (56) can be written as the following SOCP constraint for each $i \in (\mathcal{B}_m \cup \hat{\mathcal{B}}_m)$ and $m \in \mathcal{M}$:

$$\left(\kappa^{PC}_{mi}\right)^2 \left(\frac{C_{mii}+1}{2}\right)^2 \geq \left(\kappa^{PC}_{mi}\right)^2 \left(\frac{C_{mii}-1}{2}\right)^2 + \left(\frac{p^D_{mi}}{\overline{p}^D_{mi}} - \kappa^{PI}_{mi} C_{mii} - \kappa^{PP}_{mi}\right)^2. \tag{57}$$

□

5.1.3 Linearizion of the Bilinear Terms

Finally, let us linearize the bilinear terms $x_{mi} p^D_{mi}$ and $x_{mi} q^D_{mi}$ in (16)-(19) and (40), where each bilinear term involves the product of a binary variable and a nonnegative continuous variable. We linearize these disjunctive terms via the big-M method by introducing auxiliary semi-continuous variables $\rho_{mi} := x_{mi} p^D_{mi}$ and $\sigma_{mi} := x_{mi} q^D_{mi}$ and defining additional constraints for each $i \in (\mathcal{B}_m \cup \hat{\mathcal{B}}_m)$ and $m \in \mathcal{M}$:

$$-\left(1 - x_{mi}\right) \check{M}^p_{mi} \leq \rho_{mi} - p^D_{mi} \leq \check{M}^p_{mi} \left(1 - x_{mi}\right), \tag{58a}$$

$$-x_{mi} \check{M}^p_{mi} \leq \rho_{mi} \leq \check{M}^p_{mi} x_{mi}, \tag{58b}$$

$$-\left(1 - x_{mi}\right) \check{M}^q_{mi} \leq \sigma_{mi} - q^D_{mi} \leq \check{M}^q_{mi} \left(1 - x_{mi}\right), \tag{58c}$$

$$-x_{mi} \check{M}^q_{mi} \leq \sigma_{mi} \leq \check{M}^q_{mi} x_{mi}. \tag{58d}$$

In order to reduce the integrality gap in (58), the big-Ms (i.e., $\check{M}^p_{mi}$ and $\check{M}^q_{mi}$) should be as small as possible, and it is usually challenging to determine correct values for them to use for each specific implementation. However, in this particular application, we can set $\check{M}^p_{mi} = \overline{p}^D_{mi}$ and $\check{M}^q_{mi} = \overline{q}^D_{mi}$. Note that these data (i.e., the upper bounds of active and reactive loads) are usually available in any system. Now, substituting the auxiliary variables ρ_{mi} and σ_{mi} into the constraints (16)-(19), we get the linear constraints (59a)-(59b) for each $m \in \mathcal{M}$, $i \in \mathcal{B}_m$, and also the constraints (59c)-(59d) for each $m \in \mathcal{M}$, $i \in \hat{\mathcal{B}}_m$:

$$\sum_{g:(g,i)\in\mathcal{O}_m} p^G_{mg} - \rho_{mi} = \sum_{(i,j)\in\mathcal{L}_m} f^P_{mij}, \tag{59a}$$

$$\sum_{g:(g,i)\in\mathcal{O}_m} q^G_{mg} - \sigma_{mi} = \sum_{(i,j)\in\mathcal{L}_m} f^Q_{mij}, \tag{59b}$$

$$\sum_{g:(g,i)\in\mathcal{O}_m} p^G_{mg} - \rho_{mi} + \Delta P_m = \sum_{(i,j)\in\mathcal{L}_m} f^P_{mij}, \tag{59c}$$

$$\sum_{g:(g,i)\in\mathcal{O}_m} q^G_{mg} - \sigma_{mi} + \Delta Q_m = \sum_{(i,j)\in\mathcal{L}_m} f^Q_{mij}. \tag{59d}$$

Complementarily, the frequency constraints (40) can be written as (60) for each $\mathcal{S} \subseteq \tilde{\mathcal{N}}, \mathcal{S} \neq \emptyset$, where the indicator function $\mathcal{I}_M$ is modeled using the big-M method and the bilinear terms are replaced with their linear counterparts:

$$\Delta\omega_N^{\min} \leq \alpha_{\mathcal{S}} \sum_{m \in \tilde{\mathcal{B}}_{\mathcal{S}}} \left(-\Delta P_m^0 + \sum_{i \in \mathcal{B}_m} \left(p_{mi}^D - \rho_{mi} \right) \right) + \sum_{(m,k) \in \tilde{\mathcal{L}}(\mathcal{S})} (1 - Z_{mk}) M_N + \sum_{(m,k) \in \delta(\mathcal{S})} (Z_{mk}) M_N, \tag{60a}$$

$$\Delta\omega_N^{\max} \geq \alpha_{\mathcal{S}} \sum_{m \in \tilde{\mathcal{B}}_{\mathcal{S}}} \left(-\Delta P_m^0 + \sum_{i \in \mathcal{B}_m} \left(p_{mi}^D - \rho_{mi} \right) \right) - \sum_{(m,k) \in \tilde{\mathcal{L}}(\mathcal{S})} (1 - Z_{mk}) M_N - \sum_{(m,k) \in \delta(\mathcal{S})} (Z_{mk}) M_N, \tag{60b}$$

$$\Delta\omega_{ss}^{\min} \leq \beta_{\mathcal{S}} \sum_{m \in \tilde{\mathcal{B}}_{\mathcal{S}}} \left(-\Delta P_m^0 + \sum_{i \in \mathcal{B}_m} \left(p_{mi}^D - \rho_{mi} \right) \right) + \sum_{(m,k) \in \tilde{\mathcal{L}}(\mathcal{S})} (1 - Z_{mk}) M_{ss} + \sum_{(m,k) \in \delta(\mathcal{S})} (Z_{mk}) M_{ss}, \tag{60c}$$

$$\Delta\omega_{ss}^{\max} \geq \beta_{\mathcal{S}} \sum_{m \in \tilde{\mathcal{B}}_{\mathcal{S}}} \left(-\Delta P_m^0 + \sum_{i \in \mathcal{B}_m} \left(p_{mi}^D - \rho_{mi} \right) \right) - \sum_{(m,k) \in \tilde{\mathcal{L}}(\mathcal{S})} (1 - Z_{mk}) M_{ss} - \sum_{(m,k) \in \delta(\mathcal{S})} (Z_{mk}) M_{ss}. \tag{60d}$$

5.1.4 Overall MISOCP Formulation

Before proceeding further with the analysis, let us define the set $\mathcal{R}$ as the set of constraints (22), (26), (27), (32)-(34), (36)-(39), (45b), (46b), (47)-(51), (53), (54), (58), and (59). Recall that $\mathcal{F}$ is the set of frequency constraints. Now, we can formally define $\mathcal{MISOCP}(\mathcal{R}, \mathcal{F})$, as the MISOCP relaxation of the multi-μG resilient operation problem:

$$\begin{aligned} \psi = \min \; & \sum_{m \in \mathcal{M}} \sum_{i \in \mathcal{B}_m} \lambda_{mi}^{VOLL} \left(1 - x_{mi}\right) \bar{p}_{mi}^D \\ \text{s.t.} \quad & (22), (26), (27), (32)\text{-}(34), (36)\text{-}(39), (45b), \\ & (46b), (47)\text{-}(51), (53), (54), (58)\text{-}(60). \end{aligned}$$

It remains to deal with the exponential number of constraints in $\mathcal{F}$. This is the topic of the next section.

5.2 Cutting Plane Algorithm for Frequency Constraints

In this section, we propose a cutting plane approach to solve $\mathcal{MISOCP}(\mathcal{R}, \mathcal{F})$. The idea is to construct $\{\mathcal{F}_k\}_{k \geq 0}$, that is a sequence of relaxations of the set $\mathcal{F}$, and dynamically update $\mathcal{F}_k$ to obtain stronger relaxations in each iteration. Recall that the set $\mathcal{F}$ contains exponentially many frequency constraints.

With this aim in mind, let $\mathcal{C}_{\mathcal{S}}^1$, $\mathcal{C}_{\mathcal{S}}^2$, $\mathcal{C}_{\mathcal{S}}^3$, and $\mathcal{C}_{\mathcal{S}}^4$ denote respectively the constraints (60a), (60b), (60c), and (60d), for a given connected component $\mathcal{S}$ of the linking grid, where

Algorithm 1 Multi-μG resilient operation algorithm

Initialize $k \leftarrow 0$, $\mathcal{F}_k \leftarrow \emptyset$, Flag $\leftarrow$ `NO`
while Flag = `NO` **do**
  Solve $\mathcal{MISOCP}(\mathcal{R}, \mathcal{F}_k)$ to obtain the graph $\tilde{\mathcal{N}}^*$ representing the optimal configuration of the linking grid
  Compute $\mathcal{Q} = \{\mathcal{S}_{\upsilon_1}, \mathcal{S}_{\upsilon_2}, ..., \mathcal{S}_{\upsilon_N}\}$ as the set of connected components of $\tilde{\mathcal{N}}^*$
  Flag $\leftarrow$ `YES`
  for $\upsilon = \upsilon_1$ **to** υ_N **do**
    for $\gamma = 1$ **to** 4 **do**
      if $\mathcal{S}_\upsilon$ violates $\mathcal{C}^\gamma_{\mathcal{S}_\upsilon}$ **then**
        Flag $\leftarrow$ `NO`
        $\mathcal{F}_k \leftarrow \mathcal{F}_k \cup \{\mathcal{C}^\gamma_{\mathcal{S}_\upsilon}\}$
      end if
    end for
  end for
  $k \leftarrow k + 1$
end while

$\mathcal{S} \subseteq \tilde{\mathcal{N}}, \mathcal{S} \neq \emptyset$. Moreover, let the graph $\tilde{\mathcal{N}}^*$ represent the configuration of the linking grid for a given solution to $\mathcal{MISOCP}(\mathcal{R}, \mathcal{F}_k)$, and let $\mathcal{Q} = \{\mathcal{S}_{\upsilon_1}, \mathcal{S}_{\upsilon_2}, ..., \mathcal{S}_{\upsilon_N}\}$ denote the set of connected components of $\tilde{\mathcal{N}}^*$ where $\{\upsilon_1, \upsilon_2, ..., \upsilon_N\} \subseteq \{1, 2, ..., |\tilde{\mathcal{B}}|\}$. For each component in $\mathcal{Q}$, we check the inequalities $\{\mathcal{C}^\gamma_{\mathcal{S}}\}^4_{\gamma=1}$; if any frequency violation is detected, the corresponding valid inequality will be added to the set $\mathcal{F}_k$. In other words, let $\mathcal{A}$ be the set of feasible solutions to the problem $\mathcal{MISOCP}(\mathcal{R}, \mathcal{F})$. In each iteration, if an optimal solution of $\mathcal{MISOCP}(\mathcal{R}, \mathcal{F}_k)$ is in the set $\mathcal{A}$, we stop since we have already found an optimal solution to $\mathcal{MISOCP}(\mathcal{R}, \mathcal{F})$. Otherwise, we generate a cut and add it to $\mathcal{F}_k$ to separate the point from the set $\mathcal{A}$ and obtain stronger relaxations in the next iteration. Algorithm 1 provides the details of the proposed cutting plane approach.

As can be seen, in Algorithm 1, we need a function to return the connected components of the undirected graph $\tilde{\mathcal{N}}^*$. Recall that a connected component of an undirected graph is a maximal connected subgraph of the graph. This function can be implemented via depth-first or breadth-first algorithm. See [19] for details.

Theorem 1. *Algorithm 1 converges to an optimal solution of the MISOCP-based multi-μG resilient operation problem, i.e., $\mathcal{MISOCP}(\mathcal{R}, \mathcal{F})$, in a finite number of iterations.*

Proof. Let x^*_{mi} and Z^*_{mk} be an optimal solution to the problem $\mathcal{MISOCP}(\mathcal{R}, \mathcal{F}_0)$ where $i \in (\mathcal{B}_m \cup \hat{\mathcal{B}}_m), m \in \mathcal{M}$, $(m, k) \in \tilde{\mathcal{L}}$, and $\mathcal{F}_0 = \emptyset$. If x^*_{mi} and Z^*_{mk} satisfy (60), then Algorithm 1 converges to the optimal solution in one iteration. Otherwise, in each iteration, at least one constraint will be added to the set $\mathcal{F}_k$. We observe that the total number of constraints in (60) is $4r$, where r is the number of possible connected components of $\tilde{\mathcal{N}}$. Since each connected component is examined at most once in this algorithm, the number of iterations needed for the convergence of the algorithm is less than $4r$. □

6 Computational Experiments

In this section, the performance of the proposed framework for the multi-μG resilient operation problem is thoroughly evaluated. All simulations are conducted on a 64-bit PC with Intel Core i7 CPU 2.8 GHz processor and 16 GB RAM. The algorithm is implemented in the GAMS IDE environment [20]. We use BONMIN V1.8 [21] to solve MINLPs and CPLEX V12.4 [22] to solve the MISOCPs. Moreover, we use the 39-bus multi-μG network (depicted in Fig. 1) as our test system. This network is composed of six DERs, whose technical data are given in Table 1. Feeders' and loads' data are adopted from different portions of a standard IEEE distribution test system whose data can be found in [23]. To have a more realistic study, five different load types (i.e., general, residential, agricultural, commercial, and industrial) with different VOLLs are taken into account (see Fig. 5 in [13]). Finally, the μGs' dynamic data is given in Table 2.

Table 1: Technical Data of DERs

	DERs					
Parameters	G_1	G_2	G_3	G_4	G_5	G_6
$p^{G,\min}$ [$\times$100 kW]	1	1	1	1	1	1
$p^{G,\max}$[$\times$100 kW]	5	2	5	2	2	5
$q^{G,\min}$[$\times$100 kVAr]	-5	-2	-5	-2	-2	-5
$q^{G,\max}$[$\times$100 kVAr]	5	2	5	2	2	5
$R^D \backslash R^D$[$\times$100 kW/min]	2	1	2	1	1	2

Table 2: Dynamic Parameters of the VSC Controller in each μG

Parameter	Value	Parameter	Value	Parameter	Value
H [sec.]	0.9	D	1	T' [sec.]	0.1
R	0.08	$\Delta\omega_N$ [Hz]	0.5	V_{Base}[kV]	12.66
T [sec.]	0.008	$\Delta\omega_{ss}$ [Hz]	0.1	S_{Base}[MW]	5

We assume that all μGs in Fig. 1 were initially connected to the main grid through the dashed lines (in red). Subsequent to islanding, these lines along with the main circuit breaker trip. The proposed MISOCP-based resilient operation approach determines the optimal strategy which may include re-closing the dashed lines and switching the dotted lines (in gray), leading to different configurations for the distribution network. In order to evaluate our framework, we compare it with the following two schemes:

- *MINLP-Based Scheme:* In this scheme, we follow our resilient operation scheme; however, we use $\mathcal{MINLP}(\mathcal{X}, \mathcal{F})$ as the decision support tool in Algorithm 1.
- *Conventional UFLS Scheme:* In this scheme, subsequent to islanding of the distribution network, each μG individually enters the island mode where the conventional UFLS relays will curtail the necessary blocks of loads until reaching the equilibrium point. The settings of these relays are obtained from [13] and [24].

6.1 Comparison with the MINLP-Based Scheme

6.1.1 Solution and Computation Time

Table 3 provides a comparison between the MINLP-based and MISOCP-based schemes considering different severities for the islanding event (we define severity as the amount of power flow from the main grid to the distribution network before the islanding). The computation times in this table are obtained using a relative optimality criterion (i.e., Optcr) of zero.

As can be seen, although the computation time is considerably diminished in the MISOCP-based model, the solution quality (in terms of load curtailment) is the same, and this is highly effective in precarious situations such as the emergency management of distribution networks, since prompt measures can keep electromechanical dynamics away from becoming stability threatening.

Table 3: Comparison Between the MISOCP and MINLP Models

Islanding Severity [kW]	**MISOCP-Based Scheme**		**MINLP-Based Scheme**	
	Curtailment [kW]	Computation time [sec.]	Curtailment [kW]	Computation time [sec.]
2700	2248.4	57.21	2248.8	2978.8
3200	2725	52.74	2725	7185.7
3700	3208.4	73.58	3209.4	9593.5

6.1.2 Convergence

In order to see more details about the convergence of Algorithm 1, let us analyze the second islanding event (with the severity of 3200 kW). For this event, Table 4 provides the objective function value, the cardinality of the set $\mathcal{F}_k$, the amount of load shedding, the configuration of the multi-μG network, and the elapsed time in each iteration of the algorithm while solving $\mathcal{MISOCP}(\mathcal{R}, \mathcal{F})$. Accordingly, the algorithm converges in 15 iterations. In each iteration, a set of cuts are generated to separate a given solution of $\mathcal{MISOCP}(\mathcal{R}, \mathcal{F}_k)$, that is a mixed integer solution, from the set $\mathcal{A}$. This separation in each iteration leads to an interplay between load shedding adjustments and network topology control, demonstrated in the 4^{th} and 5^{th} columns of Table 4. It must be emphasized that when a mixed integer solution is cut off, the corresponding integer solution (i.e., the projection onto the space of integer variables) may not be cut off. For instance, in the 7^{th} iteration in in Table 4, the amount of load shedding is 2295 kW and the connected edges of the linking grid are l_1, l_3, and l_5 (see Fig. 1(b)). Although a valid inequality cuts off this mixed integer solution in the next iteration, the corresponding integer solution appears again in the 15^{th} iteration with a different amount of load shedding.

As another interesting result, in the eighth iteration, the distribution network is partitioned into two sub-systems and the objective function is increased by 8.5%. Eventually, in the 15^{th} iteration, the optimal resilience improvement strategy is achieved while the distribution system is reconfigured as one connected component.

For the sake of comparison, Table 5 provides the outputs of Algorithm 1 while solving $\mathcal{MINLP}(\mathcal{X}, \mathcal{F})$. As can be seen, the algorithm converges in a more number of iterations

and the computation time of each iteration is considerably more than that of the MISOCP-based model. The final solutions (the objective function, load curtailment, and configuration of the linking grid), nevertheless, are quite the same as the ones in Table 4.

Table 4: Convergence Process of the Proposed Algorithm While Solving $\mathcal{MISOCP}(\mathcal{R}, \mathcal{F})$

k	ψ [$\times$100 \$]	$\lvert\mathcal{F}_k\rvert$	Curtailment [$\times$100 kW]	Connected edges of $\tilde{\mathcal{N}}$	Elapsed time/iter [sec.]
0	1579.09	0	22.98	l_1, l_2, l_3	6.0
1	1579.09	1	22.93	l_2, l_4, l_5	3.8
2	1579.09	2	22.91	l_2, l_3, l_4	4.0
3	1579.09	3	23.07	l_1, l_3, l_4	4.6
4	1579.09	4	22.87	l_3, l_4, l_5	3.2
5	1579.09	5	22.93	l_1, l_2, l_5	2.9
6	1579.09	6	23.03	l_1, l_2, l_4	2.6
7	1579.09	7	22.95	l_1, l_3, l_5	2.7
8	1714.69	8	23.40	l_2, l_3, l_5	1.6
9	2069.38	10	24.29	l_1, l_4	5.9
10	2081.35	12	24.92	l_1, l_5	3.9
11	2081.35	13	24.92	l_4, l_5	2.0
12	2086.23	14	24.11	l_2, l_5	2.4
13	2086.23	15	24.15	l_3, l_5	2.2
14	2086.23	16	24.07	l_2, l_3	2.7
15	2235.96	17	27.25	l_1, l_3, l_5	2.4

6.2 Comparison with the Conventional UFLS Scheme

Fig. 4 provides a comparison between the MISOCP-based scheme and the conventional UFLS scheme while they are coping with the second islanding event (with severity of 3200 kW). To have a more realistic result, we assume the communication latency to be 100 ms in the proposed scheme. We also consider the intentional delay of the UFLS relays to be 100 ms. Since the distribution network is partitioned into four μGs in the conventional UFLS scheme, this figure compares the amount of load shedding, nadir frequency, and steady state frequency in each μG (denoted by m_1 to m_4), on the one hand, and the same indices in the multi-μG network which is obtained from the proposed MISOCP-based scheme, on the other hand.

Accordingly, the total amount of load shedding in our proposed scheme is 2725 kW, while the steady state and nadir frequencies are remained within the permissible range. In comparison, the total amount of load shedding in the conventional scheme is 3700 kW (even more than the initial power deficiency), and the frequency of the μGs violates the safe range. Specifically, in m_3, the violation of frequency is more serious, and the conventional scheme fails to maintain the frequency stability of the network. The main reason for this observation is the rigidity of the conventional UFLS scheme in dealing with different contingencies. In this scheme, load shedding is implemented in several steps with fixed sizes, regardless of the intensity of the islanding. Therefore, it can be inferred that the conventional method sheds non-optimal amount of loads encountering islanding events. These results illustrate that the proposed method is capable of preserving the distribution network from collapsing and

Table 5: Convergence Process of the Proposed Algorithm While Solving $\mathcal{MINLP}(\mathcal{X}, \mathcal{F})$

k	ϑ [$\times$100 \$]	$\lvert\mathcal{F}_k\rvert$	Curtailment [$\times$100 kW]	Connected edges of $\tilde{\mathcal{N}}$	Elapsed time/iter [sec.]
0	1579.09	0	22.89	l_1, l_3, l_4	664.2
1	1579.09	1	22.88	l_1, l_2, l_4	478.1
2	1579.09	2	22.87	l_1, l_2, l_3, l_5	391.9
3	1579.09	3	22.86	l_1, l_2, l_5	329.8
4	1579.09	4	22.87	l_2, l_3, l_4, l_5	341.4
5	1579.09	5	22.84	l_2, l_4, l_5	246.3
6	1579.09	6	22.86	l_1, l_3, l_5	285.5
7	1579.09	7	22.83	l_3, l_4, l_5	185.0
8	1579.09	8	22.86	l_1, l_2, l_3	165.0
9	1579.09	9	22.86	l_2, l_3, l_4	124.1
10	1714.69	10	23.14	l_2, l_3, l_5	291.7
11	2069.38	12	24.06	l_1, l_4	516.6
12	2081.35	14	24.68	l_1, l_5	387.5
13	2081.35	15	24.71	l_4, l_5	353.4
14	2086.23	16	23.86	l_2, l_5	322.2
15	2086.23	17	23.88	l_3, l_5	530.0
16	2086.23	18	23.89	l_2, l_3	172.6
17	2235.96	19	27.25	l_1, l_3, l_4	1400.7

moving it to a new steady state and stable condition. It is worth mentioning that, aside from the COI frequency, keeping the bus voltages and line flows within the permissible range in our proposed scheme would guarantee a secure operation following the islanding process, which is not considered in the conventional scheme.

7 Conclusions

In this paper, we propose a novel framework for the near real-time operation as well as the real-time control of multi-μG networks. Our framework provides the optimal power flow, optimal load shedding, and optimal topology reconfiguration, while frequency dynamics and AC power flow limitations are taken into account. An exact reformulation of frequency constraints in a cutting plane algorithm with tight MISOCP relaxations is established, which significantly speeds up computation and achieves near optimal solution. To the best of our knowledge, this comprehensive optimization and control framework for the frequency stability of multi-μGs is proposed for the first time in the literature. Our numerical experiments further illustrate that the proposed emergency control scheme can successfully monitor, verify, and act to guarantee that the multi-μG network remains within the operational limits during post-islanding frequency dynamics. It is practical for real-world applications and outperforms the conventional UFLS scheme in terms of load shedding amount, number of curtailed customers, and frequency stability.

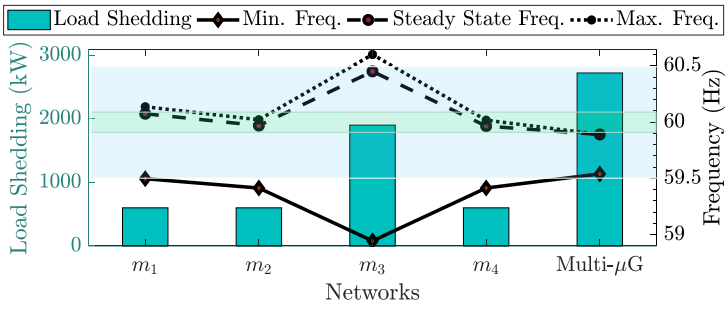

Figure 4: Comparison between the proposed MISOCP-based and conventional UFLS schemes for an islanding event with severity of 3200 kW. Permissible ranges of nadir and steady state frequencies are shown by horizontal bars.

References

[1] *IEEE Recommended Practice for Utility Interconnected Photovoltaic (PV) Systems*, IEEE Std. 929-2000, 2000.

[2] *IEEE Guide for Conducting Distribution Impact Studies for Distributed Resource Interconnection*, IEEE Std. 1547.7-2013, Dec. 2013.

[3] *IEEE Draft Standard for Interconnection and Interoperability of Distributed Energy Resources with Associated Electric Power Systems Interfaces*, IEEE P1547/D6.7.2, May 2017.

[4] P. Mahat, Z. Chen, and B. Bak-Jensen, "Under frequency load shedding for an islanded distribution system with distributed generators," *IEEE Trans. Power Del.*, vol. 25, no. 2, pp. 911–918, Apr. 2010.

[5] F. Katiraei, M. R. Iravani, and P. W. Lehn, "Micro-grid autonomous operation during and subsequent to islanding process," *IEEE Trans. Power Del.*, vol. 20, no. 1, pp. 248–257, 2005.

[6] I. J. Balaguer, Q. Lei, S. Yang, U. Supatti, and F. Z. Peng, "Control for grid-connected and intentional islanding operations of distributed power generation," *IEEE Trans. Ind. Electron.*, vol. 58, no. 1, pp. 147–157, 2011.

[7] Y. Zhang and L. Xie, "Online dynamic security assessment of microgrid interconnections in smart distribution systems," *IEEE Trans. Power Syst.*, vol. 30, no. 6, pp. 3246–3254, 2015.

[8] Y. Zhang, L. Xie, and Q. Ding, "Interactive control of coupled microgrids for guaranteed system-wide small signal stability," *IEEE Trans. Smart Grid*, vol. 7, no. 2, pp. 1088–1096, 2016.

[9] Y. Zhang and L. Xie, "A transient stability assessment framework in power electronic-interfaced distribution systems," *IEEE Trans. Power Syst.*, vol. 31, no. 6, pp. 5106–5114, 2016.

[10] W.-Y. Chiu, H. Sun, and H. V. Poor, "A multiobjective approach to multimicrogrid system design," *IEEE Trans. Smart Grid*, vol. 6, no. 5, pp. 2263–2272, 2015.

[11] H. Farzin, M. Fotuhi-Firuzabad, and M. Moeini-Aghtaie, "Enhancing power system resilience through hierarchical outage management in multi-microgrids," *IEEE Trans. Smart Grid*, vol. 7, no. 6, pp. 2869–2879, 2016.

[12] Z. Wang, B. Chen, J. Wang, and C. Chen, "Networked microgrids for self-healing power systems," *IEEE Trans. Smart Grid*, vol. 7, no. 1, pp. 310–319, 2016.

[13] A. Gholami, T. Shekari, and A. Sun, "An adaptive optimization-based load shedding scheme in microgrids," in *Proceedings of the 51st Hawaii International Conference on System Sciences*, 2018.

[14] R. Majumder, A. Ghosh, G. Ledwich, and F. Zare, "Power management and power flow control with back-to-back converters in a utility connected microgrid," *IEEE Trans. Power Syst.*, vol. 25, no. 2, pp. 821–834, 2010.

[15] P. Kundur, *Power system stability and control*. McGraw–hill, New York, 1994.

[16] H. Ahmadi and H. Ghasemi, "Security-constrained unit commitment with linearized system frequency limit constraints," *IEEE Trans. Power Syst.*, vol. 29, no. 4, pp. 1536–1545, 2014.

[17] F. Paganini and E. Mallada, "Global performance metrics for synchronization of heterogeneously rated power systems: The role of machine models and inertia," *ArXiv e-prints*, Oct. 2017.

[18] B. Kocuk, S. S. Dey, and X. A. Sun, "Strong SOCP relaxations for the optimal power flow problem," *Oper. Res.*, vol. 64, no. 6, pp. 1177–1196, 2016.

[19] D. B. West *et al.*, *Introduction to graph theory*. Prentice hall Upper Saddle River, 2001, vol. 2.

[20] (2016) GAMS User Manual. [Online]. Available: https://www.gams.com

[21] (2007) BONMIN User Manual. [Online]. Available: https://www.coin-or.org

[22] (2016) CPLEX User Manual. [Online]. Available: https://www.ibm.com

[23] M. E. Baran and F. Wu, "Network reconfiguration in distribution system for loss reduction and load balancing," *IEEE Trans. Power Del.*, vol. 4, no. 2, pp. 1401–1407, Apr. 1989.

[24] M. Abedini, M. Sanaye-Pasand, and S. Azizi, "Adaptive load shedding scheme to preserve the power system stability following large disturbances," *IET Gen. Transm. Distrib.*, vol. 8, no. 12, pp. 2124–2133, Dec. 2014.